The use of inverse methods for response estimation of long-span suspension bridges with uncertain wind loading conditions

Practical implementation and results for the Hardanger Bridge

Petersen, Øyvind Wiig; Oiseth, Ole; Lourens, Eliz-Mari

DOI
10.1007/s13349-018-0319-y

Publication date
2018

Document Version
Accepted author manuscript

Published in
Journal of Civil Structural Health Monitoring

Citation (APA)
Petersen, Ø. W., Oiseth, O., & Lourens, E.-M. (2018). The use of inverse methods for response estimation of long-span suspension bridges with uncertain wind loading conditions: Practical implementation and results for the Hardanger Bridge. *Journal of Civil Structural Health Monitoring*, *9*(1), 21-36. https://doi.org/10.1007/s13349-018-0319-y

Journal of Civil Structural Health Monitoring manuscript No.
(will be inserted by the editor)

The use of inverse methods for response estimation of long-span suspension bridges with uncertain wind loading conditions

Practical implementation and results for the Hardanger Bridge

Øyvind Wiig Petersen · Ole Øiseth · Eliz-Mari Lourens

Received: date / Accepted: date

Abstract Structural health monitoring (SHM) seeks to assess the condition or behaviour of the structure from measurement data, which for long-span bridges typically are wind velocities and/or structural vibrations. However, in the assessment of the wind-induced response effects, models for the actual loads must be adopted, which introduces uncertainties. An alternative is to apply model-based inverse methods that consider the input forces unknown, and estimate these forces jointly together with the system states using limited vibration data. This article presents a case study of implementing Kalman-type inverse methods to a long-span suspension bridge in complex terrain, with the objective of estimating the full-field response. Previous studies have shown the local wind field is complicated, leading to uncertain load effects. We discuss the key challenges faced in the use of the methodology for the long-span bridges and present the results for a six hour storm event. The analysis show that the dynamic response contribution from the 14 lowermost bridge modes (up to 3 rad/s or 0.5 Hz) can be reconstructed with decent accuracy. The estimated response magnitude differs from the predicted response from design specifications, pointing to initial load model uncertainties that can be reduced to give greater confidence in the assessment of wind-induced fatigue, wind-resistant performance or other response effects.

Keywords Suspension bridge · structural monitoring · inverse methods · response estimation

1 Introduction

Bridges are an important part of societal infrastructure, and it is vital that these structures can operate with sufficient structural safety. The past two decades have witnessed improvements in computational and sensor technology, leading to increasing interest in structural health monitoring (SHM) using in-situ measurements as a tool for assessing the condition of a structure.

For long-span bridges, which are generally of the cable-supported type, it is common to use measured vibration data from ambient excitation, such as traffic or wind. The vibration data are typically acquired in the form of accelerations or strains but can be supplemented by additional measurements, such as temperature, GPS, wind velocity or local traffic. The review in [16] outlines many of the trends in SHM of large-scale bridges. A more recent state-of-the-art review with a focus on cable-stayed bridges is provided in [18]. The survey on vibration-based SHM in [4] collects many of the success stories but also points to one of the difficulties in classic damage detection in large bridges: the global modal characteristics are not sensitive to local damage, and the measurements will always contain natural variations in the modal data due to circumstantial causes such as wind, traffic and temperature. Although (numerical) studies have focused on frameworks for elimination of environmental effects through novelty detection by principal component analysis [7,8] or neural networks [17,27], the authors of this paper still believe that vibration-based direct detection of damage remains highly difficult for in-operation suspension bridges due to the number of environmental conditions that remain unknown or uncontrollable. Therefore, this paper considers the improvement of response estimation for reliable analysis of response effects in long-span bridges, that could be developed as a tool for the assessment of condition of the structure.

In SHM frameworks, the assessment of bridge response effects may take several forms, depending on the type of available data. The works in [12,36] considered buffeting-induced fatigue damage based on a probabilistic distribution of wind velocities and directions from on-site wind data. An observation recognized in these studies is that the complexity and inaccuracy of the joint probabilistic distributions could lead to serious errors the estimated fatigue damage. Another approach to fatigue life assessment is to use direct strain data collected under various wind and traffic conditions [6,38],

Ø.W. Petersen · O. Øiseth
NTNU, Norwegian University of Science and Technology, NO-7491 Trondheim, Norway
E-mail: oyvind.w.petersen@ntnu.no

E. Lourens
Delft University of Technology, 2628 CN Delft, The Netherlands

i.e. creating a long-term statistical response model. In [39] it was addressed the stochastic characterization of the local wind field from wind monitoring data, with the aim to facilitate the structural performance evaluation of long-span bridges under wind action. Although many of the current SHM systems feature wind measurements and provide information on common wind field parameters (mean velocity, turbulence, direction, angle of attack, spectral shape, correlations), the wind loads are not directly measured, as pointed out in [37].

The absence of direct load data inevitable necessitates a set of adopted load assumptions, which may be an obstacle to the reliability of the assessment. This has driven the development of the class of inverse methods that that consider the excitation forces unknown, and estimate these forces jointly together with the system states (displacements/velocities), using a system model and measured vibration data. Several different techniques have already been implemented in real-life structures. As already proposed by researchers, this can be applied to, for example, monitor fatigue in wind turbine foundations in [14,15,23] and off-shore jackets [32], to study wind forces on tall buildings [41] and ice forces on lighthouses [28]. In these cases, the environmental (wind, wave or ice) forces present are uncertain, either due to their inherent stochastic nature or because the mechanics behind the load interaction is unclear.

The use of the inverse methods has however seen little exploration for long-span bridges, which is what this paper focuses on. Although the general methodology applied in this contribution is well-known [1,20,25], the application to long-span bridges under environmental loading is new, where the wind loads are governed by the local wind field and the aerodynamic properties of the structure, both of which are not always well-known. Local wind measurements at bridge sites often indicate a variability (non-deterministic scatter) in the parameters used to described the wind field [11,13], which sometimes also deviates from recommended values in design specifications [3,35]. This leads to a discrepancy between the measured and predicted response, as observed in [9,34]. Due to the structural size, the spatial properties of the wind field is also an important but often uncertain aspect due to the limited number of points at which the wind is measured, especially before the bridge is built. Inverse methods could therefore be used to reduce the response effect uncertainties in long-span bridges by making use of the measurement data rather than relying on predictions from a generic load model. Calibration of existing load models is also a possible opportunity. This will in turn lead to a more reliable representation of the dynamic behavior, which is key in assessments of wind-induced fatigue and wind-resistant design.

In reliability-based design, uncertainties are generally met with conservative measures, but in practice, this is also balanced with cost and design feasibility. The uncertainties play a role in assessment of structural safety, serviceability and maintenance strategies of the infrastructure. This points to the knowledge gain from monitoring these structures through their lifetime.

This paper presents a case study on a suspension bridge, the Hardanger Bridge, extending some of the results from [30]. The bridge case-study is representative for other (existing or future) bridges located in complex terrains, for example in fjord-mountain or strait-island areas. A shared trait for these structures is that the load effects from wind are challenging to characterize accurately. Results from the monitoring at Hardanger Bridge shows that the numerical predictions of buffeting response based on design wind spectra are underestimated compared to the measurements [9]. The same study also showed that the wind-related parameters turbulence intensity, length scales, angle of attack and coherence decay coefficients had a considerable variability, which is typically is not considered in design predictions. The predicted dynamic behaviour also relies on aerodynamic models calibrated from wind tunnel experiments using scale section models [31], an exercise that also involves simplifications and uncertainties that may not match the real-life behaviour of the structure at full scale.

This article presents the implementation and feasibility of full-field response estimation in long-span bridges. Although the focus is on the results from the wind-induced response of the Hardanger Bridge, many of the presented concepts and drawn conclusions are applicable to cable-supported bridges in general.

2 Theoretical framework

2.1 Governing system equations

This section presents the relevant equations for the linear motion of bridges. The linear system formulations in this section are well-known, but is still presented to clarify how the system model and external forces are defined, since the equations of bridge dynamics can be formulated in several ways, depending on the desired application and underlying assumptions. Consider a discretized system description of a suspension bridge modelled with n_{DOF} degrees of freedom (DOFs). The structural response $\mathbf{u}(t) \in \mathbb{R}^{n_{DOF}}$ is given by the equations of motion:

$$\mathbf{M}_0\ddot{\mathbf{u}}(t) + \mathbf{C}_0\dot{\mathbf{u}}(t) + \mathbf{K}_0\mathbf{u}(t) = \mathbf{f}(t) \tag{1}$$

where $\mathbf{M}_0$, $\mathbf{C}_0$ and $\mathbf{K}_0 \in \mathbb{R}^{n_{DOF}\times n_{DOF}}$ are the mass, damping and stiffness matrices related to the structure only. The total load vector $\mathbf{f}(t) \in \mathbb{R}^{n_{DOF}}$ here consists of the wind excitation, and the vector can generally be expanded as follows:

$$\mathbf{f}(t) = \mathbf{C}_{ae}\dot{\mathbf{u}}(t) + \mathbf{K}_{ae}\mathbf{u}(t) + \mathbf{f}_B(t) + \mathbf{f}_v(t) + \mathbf{f}_s \tag{2}$$

Here, the first two terms on the right-hand side represent the motion-induced forces. There is no direct assumption imposed on the content of the aerodynamic matrices $\mathbf{C}_{ae}$ and $\mathbf{K}_{ae} \in \mathbb{R}^{n_{DOF}\times n_{DOF}}$; they can be constant (quasi-steady theory) or

frequency dependent (unsteady theory). $\mathbf{f}_\mathrm{s}$ is the static wind load, which is disregarded here since the focus is on the dynamic vibrations. $\mathbf{f}_\mathrm{B}(t)$ is the buffeting wind load due to turbulence, and $\mathbf{f}_\mathrm{v}(t)$ is the vortex-induced load, which is typically not important unless the mean wind velocity is low enough for vortex shedding lock-in vibrations to occur in the bridge deck.

Through the truncation $\mathbf{u}(t) = \boldsymbol{\Phi}\mathbf{z}(t)$, the dynamic response is represented as contributions from a limited number of modes. $\mathbf{z}(t) \in \mathbb{R}^{\mathrm{n_m}}$ is the vector of still-air modal coordinates, and $\boldsymbol{\Phi} \in \mathbb{R}^{\mathrm{n_{DOF}} \times \mathrm{n_m}}$ contains the $\mathrm{n_m}$ corresponding mass-normalized mode shapes $\boldsymbol{\phi}_j \in \mathbb{R}^{\mathrm{n_{DOF}}}$, which is solved from the still-air eigenvalue problem:

$$(\mathbf{K}_0 - \omega_j^2 \mathbf{M}_0)\boldsymbol{\phi}_j = \mathbf{0} \quad (j = 1 \ldots \mathrm{n_m}) \tag{3}$$

It is common to assume that the structural damping $\mathbf{C}_0$ can be approximated as proportional and then define $\boldsymbol{\Omega} = \mathrm{diag}(\omega_1, \omega_2, \ldots, \omega_{\mathrm{n_m}})$ and $\boldsymbol{\Xi} = \mathrm{diag}(\xi_1, \xi_2, \ldots, \xi_{\mathrm{n_m}})$; ω_j and ξ_j are the undamped natural frequency and damping ratio for mode j, respectively. The modal truncation transforms the equations of motion (Eq. 1) and now reads as follows:

$$\ddot{\mathbf{z}}(t) + 2\boldsymbol{\Xi}\boldsymbol{\Omega}\dot{\mathbf{z}}(t) + \boldsymbol{\Omega}^2\mathbf{z}(t) = \boldsymbol{\Phi}^\mathrm{T}\mathbf{f}(t) = \mathbf{p}(t) \tag{4}$$

where $\mathbf{p}(t) \in \mathbb{R}^{\mathrm{n_m}}$ are the modal forces, which in general are unknown. Since the locations of the forces on the bridge are not confined to a few discrete points, but distributed across the whole structure, a formulation using modal equivalent loads is the best alternative to account for the response of the structure [19]. Although the ambient wind loads are expected to dominate the load term, in principle, any other type of excitation on the structure, such as traffic loads, is contained within the modal load vector.

Because the system model is eventually used to process digital data, the discrete time state-space representation of Eq. 4 is used with $\mathbf{x}_k \in \mathbb{R}^{2\mathrm{n_m}}$ as the modal state vector:

$$\mathbf{x}_{k+1} = \mathbf{A}\mathbf{x}_k + \mathbf{B}\mathbf{p}_k, \quad \mathbf{x}_k = \begin{bmatrix}\mathbf{z}(t_k) \\ \dot{\mathbf{z}}(t_k)\end{bmatrix}, \quad \mathbf{p}_k = \mathbf{p}(t_k) \tag{5}$$

Here, the time axis is discretized in increments of Δt such that $t_k = k\Delta t\,(k = 0, 1, \ldots N_t - 1)$, where N_t is the number of samples. In the discretization, the forces are kept constant within each time step. It can be shown that the state transition matrix $\mathbf{A} \in \mathbb{R}^{2\mathrm{n_m} \times 2\mathrm{n_m}}$ and input matrix $\mathbf{B} \in \mathbb{R}^{2\mathrm{n_m} \times \mathrm{n_m}}$ are then given by:

$$\mathbf{A} = \exp\Big(\begin{bmatrix}\mathbf{0} & \mathbf{I} \\ -\boldsymbol{\Omega}^2 & -2\boldsymbol{\Xi}\boldsymbol{\Omega}\end{bmatrix}\Delta t\Big), \quad \mathbf{B} = (\mathbf{A} - \mathbf{I})\begin{bmatrix}\mathbf{0} & \mathbf{I} \\ -\boldsymbol{\Omega}^2 & -2\boldsymbol{\Xi}\boldsymbol{\Omega}\end{bmatrix}^{-1}\begin{bmatrix}\mathbf{0} \\ \mathbf{I}\end{bmatrix} \tag{6}$$

The system output vector $\mathbf{d}(t) \in \mathbb{R}^{\mathrm{n_d}}$ consists of accelerations and/or displacements at selected DOFs of the structure:

$$\mathbf{d}(t) = \mathbf{S}_\mathrm{a}\ddot{\mathbf{u}}(t) + \mathbf{S}_\mathrm{d}\mathbf{u}(t) \tag{7}$$

where $\mathbf{S}_\mathrm{a}$ and $\mathbf{S}_\mathrm{d} \in \mathbb{R}^{\mathrm{n_d} \times \mathrm{n_{DOF}}}$ select these DOFs. The output equation can also be formulated in state-space form:

$$\mathbf{d}_k = \mathbf{G}\mathbf{x}_k + \mathbf{J}\mathbf{p}_k \tag{8}$$

with the following output influence matrix $\mathbf{G} \in \mathbb{R}^{\mathrm{n_d} \times 2\mathrm{n_m}}$ and direct transmission matrix $\mathbf{J} \in \mathbb{R}^{\mathrm{n_d} \times \mathrm{n_m}}$:

$$\mathbf{G} = \begin{bmatrix}\mathbf{S}_\mathrm{d}\boldsymbol{\Phi} - \mathbf{S}_\mathrm{a}\boldsymbol{\Phi}\boldsymbol{\Omega}^2 & -\mathbf{S}_\mathrm{a}\boldsymbol{\Phi}2\boldsymbol{\Omega}\boldsymbol{\Xi}\end{bmatrix}, \quad \mathbf{J} = \begin{bmatrix}\mathbf{S}_\mathrm{a}\boldsymbol{\Phi}\end{bmatrix} \tag{9}$$

The stochastic-deterministic forms of Eqs. 5 and 8 read as follows:

$$\mathbf{x}_{k+1} = \mathbf{A}\mathbf{x}_k + \mathbf{B}\mathbf{p}_k + \mathbf{w}_k \tag{10}$$

$$\mathbf{d}_k = \mathbf{G}\mathbf{x}_k + \mathbf{J}\mathbf{p}_k + \mathbf{v}_k \tag{11}$$

where the zero-mean vectors $\mathbf{w}_k \in \mathbb{R}^{2\mathrm{n_m}}$ and $\mathbf{v}_k \in \mathbb{R}^{\mathrm{n_d}}$ are white noise vectors representing the process error and measurement error, which are assumed to have the following known covariance matrices:

$$\mathbb{E}[\mathbf{w}_k\mathbf{w}_l^\mathrm{T}] = \mathbf{Q}\,\delta_{kl}, \quad \mathbb{E}[\mathbf{v}_k\mathbf{v}_l^\mathrm{T}] = \mathbf{R}\,\delta_{kl}, \quad \mathbb{E}[\mathbf{w}_k\mathbf{v}_l^\mathrm{T}] = \mathbf{S}\,\delta_{kl} \tag{12}$$

Fig. 1 The Hardanger Bridge viewed from the east. Photo: NTNU/T.M. Lystad

2.2 Methods for system inversion

In this section, we summarize the prevailing stochastic-deterministic methods for system inversion. The methods combine a system model and measurement data to estimate the system states ($\hat{\mathbf{x}}_k$) and input forces ($\hat{\mathbf{p}}_k$); the hat indicates an estimated quantity. The methods may be classified as methods that make no assumption on the force evolution [20,22,25] and those that model the forces as a random walk [1,21]. The random walk equation is given as follows:

$$\mathbf{p}_{k+1} = \mathbf{p}_k + \boldsymbol{\eta}_k \tag{13}$$

where $\boldsymbol{\eta}_k \in \mathbb{R}^{2n_m}$ is a white noise vector with the covariance $\mathbb{E}[\boldsymbol{\eta}_k \boldsymbol{\eta}_l^{\mathrm{T}}] = \mathbf{Q}_{\mathrm{P}} \delta_{kl}$ working as the tuning parameter. In this paper, we employ two of the aforementioned methods: a joint input-state estimation algorithm (JIS) [20] and a dual Kalman filter (DKF) [1]. Both of these methods are Kalman-type filter algorithms, but only the latter models the forces by Eq. 13, whereas the JIS makes no specific evolution assumptions. Extensions to the filters in the form of time-delayed smoothers rather than non-instantaneous inversion have also been developed [22], but such extensions are not considered here since they mainly provide benefits when the unknown forces are strongly non-collocated.

It is not practically possible to perform direct measurements at all critical components of a structure. The number of installed sensors can be limited by cost, and the sensor locations can also be subjected to practical restrictions. As already utilized by several researchers [23,14] one of the possible solutions to this problem is the full-field response estimation using an extrapolated output equation:

$$\hat{\mathbf{d}}'_k = \mathbf{S}'_{\mathrm{d}} \hat{\mathbf{u}}_k + \mathbf{S}'_{\mathrm{a}} \hat{\ddot{\mathbf{u}}}_k = \mathbf{G}' \hat{\mathbf{x}}_k + \mathbf{J}' \hat{\mathbf{p}}_k \tag{14}$$

Here, $\mathbf{G}'$ and $\mathbf{J}'$ are constructed as defined in Eq. 9 using $\mathbf{S}'_{\mathrm{d}}$ and $\mathbf{S}'_{\mathrm{a}}$ to select the set of extrapolated DOFs. It is also possible to use Eq. 14 to predict any linear response variable, such as strains, stresses, or cross-sectional forces. This can be of interest in the indirect monitoring of fatigue or assessment of local structural demand/capacity.

The theoretical limitations and requirements for filters with instantaneous system inversion can be found in [24]. This may be summarized as three requirements concerning the observability, stability, and direct invertibility of the system. How these conditions play out for the presented case study is discussed in Section 3.3.

3 Practical implementation for the Hardanger Bridge

3.1 The Hardanger Bridge monitoring project

The Hardanger Bridge (Fig. 1) is a suspension bridge located in Norway with a main span of 1308 m. The monitoring of this bridge is part of a larger research project related to development of the E39 Coastal Highway Route, an upgrade of the main highway along the Norwegian west coast.

In this section, the focus is on the implementation of the mentioned inverse methods for the case study of the Hardanger Bridge. The methodology has both practical and theoretical limitations that must be considered; the most important points to consider are given attention.

3.2 Initial key points

Monitoring system. The bridge must be equipped with a robust and operational long-term monitoring system with either continuous data acquisition or a triggering solution that saves data from the events of interest. The monitoring system at

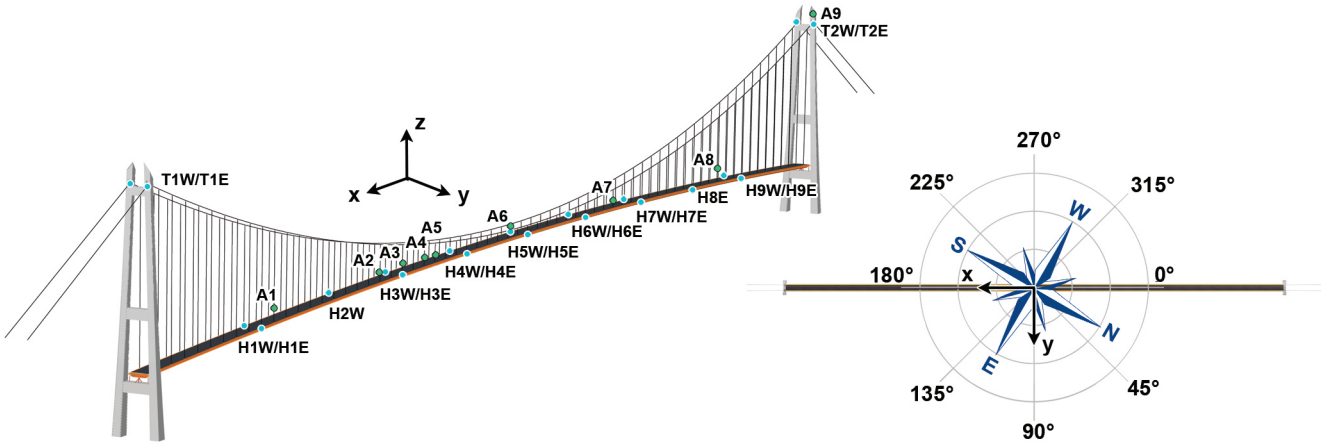

Fig. 2 Positions of sensors installed on the bridge superimposed on an FE model: anemometers (A) and accelerometers (H). The compass shows the definition of the wind direction

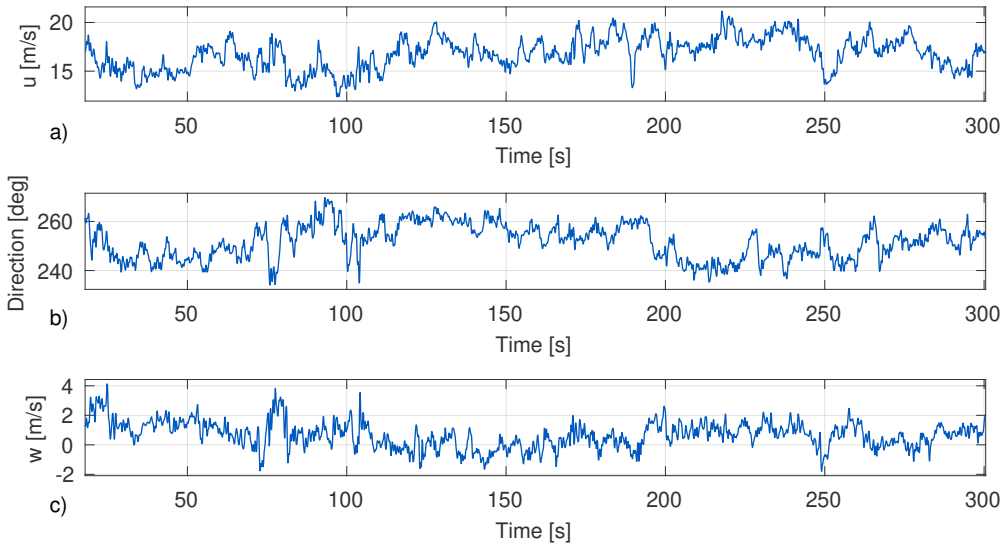

Fig. 3 Sample time series of the (a) along-wind velocity, (b) wind direction and (c) vertical wind velocity from anemometer A6

the Hardanger Bridge consists of 20 triaxial accelerometers and nine sonic anemometers at the locations shown in Fig. 2. We refer to the description in [11] for the system specifications.

Fig. 3 shows a time series (300 s window) from the midmost anemometer (A6), during a storm event that is later used as an example. For most cases, the wind approaches the bridge deck at an angle in the sectors $[60°, 150°]$ or $[250°, 300°]$ since the surrounding mountains make the wind travel along the fjord. Fig. 4 shows the simultaneously measured acceleration in the mid-span of the bridge (sensor pair H5W/H5E), transformed into lateral, vertical and torsional components.

Observed response characteristics. It is essential to have an initial overview of the dynamics of the structure under consideration. Fig. 5a-c shows the power spectral density (PSD) of a 30 minute long acceleration time series. A clear multi-modal dynamic behaviour is observable, which is a common characteristic of long-span bridges. This behaviour has implications on the number of modes needed in a system model to explain the observed data. The lowest modes tend to contribute the most to the response, however. Fig. 5d shows the acceleration variance accounted for up to a given frequency limit ω_{lim}, from the fraction:

$$\frac{\sigma^2_{\omega_{\text{lim}},n}}{\sigma^2_{\text{tot},n}} = \frac{\int_0^{\omega_{\text{lim}}} S_{\ddot{u}_n\ddot{u}_n}(\omega)\,\mathrm{d}\omega}{\int_0^{\infty} S_{\ddot{u}_n\ddot{u}_n}(\omega)\,\mathrm{d}\omega}, \quad n = \{y, z, \theta\} \tag{15}$$

where $S_{\ddot{u}_n\ddot{u}_n}(\omega)$ is the (positive) PSD of the acceleration in the lateral (y), vertical (z) or torsional (θ) DOF. For example, the spectral content below $\omega_{\text{lim}} = 3$ rad/s accounts for approximately 75% of the total acceleration variance for all three components. In terms of displacements, the fraction is greater than 99% for the same limit, indicating that low-order models can approximate the response with decent accuracy.

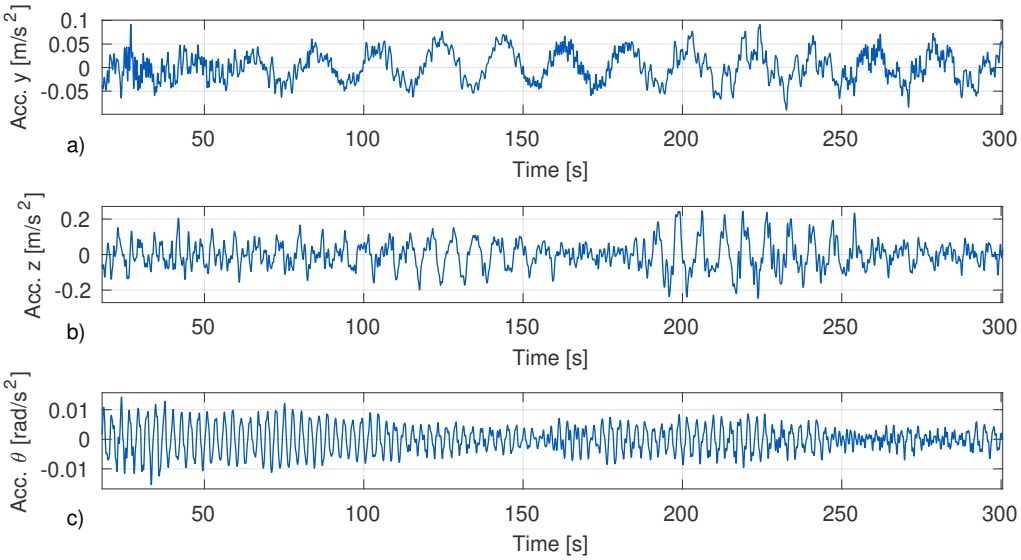

Fig. 4 Sample time series of the (a) lateral, (b) vertical and (c) torsional acceleration in the mid-span. A low-pass filter with a cut-off frequency of 12 rad/s has been applied to the data

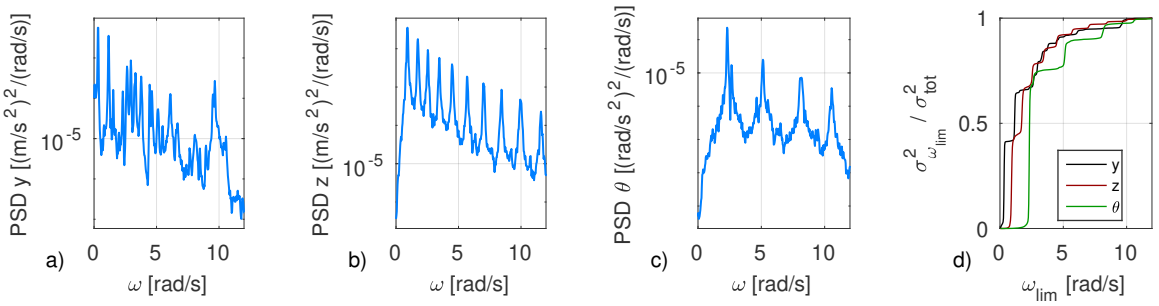

Fig. 5 Power spectral density (estimated by Welch's method) of the (a) lateral, (b) vertical and (c) torsional accelerations at the mid-span from 30 minutes of measurement data. d) Variance contribution up to the frequency limit ω_{lim}

Placement of sensors. Optimal sensor network design for SHM is a well-studied problem, which may be formulated with various objectives. Loosely speaking, the idea is to determine sensor locations, and possibly sensor types, such that the usefulness of the limited amount of data is maximized. For inverse methods that employ instantaneous system inversion, the design of the sensor network is discussed in [24]. Another direct approach is to distribute the sensors with an objective of minimizing the theoretical uncertainty of the state or force estimates in the filtering algorithms [40]; however, the result is dependent on the (assumed) noise statistics (Eq. 12), which may be incorrect or non-stationary. A basic rule of thumb is to allocate the sensors such that data are not repeated, i.e. avoiding a linear dependence between the outputs, and that all modes excited by the input should be observed. For our case, the placement of the accelerometers in Fig. 2 is already established and is not altered in this work. Note that this sensor configuration was not designed specifically for inverse problems, which leads to some shortcomings. For example, the pair-wise allocation of the sensors causes a linear dependence in the two lateral (y) components, meaning that one of the signals in each pair must be discarded because it provides no additional information. One could also argue that the (almost) symmetric accelerometer placement in Fig. 2 is not optimal since many of the modes are (almost) symmetric.

3.3 Theoretical requirements and limitations

We now discuss the most important theoretical conditions for system inversion mentioned in Section 2.2 in relation to the case study. The conditions originate from the theoretical limitations in control theory.

Observability. The observability requires that $\text{rank}((\mathbf{S}_\text{a}+\mathbf{S}_\text{d})\boldsymbol{\phi}_j) = 1$ for all $j = 1 \ldots \text{n}_\text{m}$ [24]. In general, the observability is hardly a problem since the considered modes are global and thus captured by one or more sensors in the girder.

Stability. The stability is related to the transmission zeros of the state-space model, i.e. solutions $\lambda \in \mathbb{C}$ of the equation:

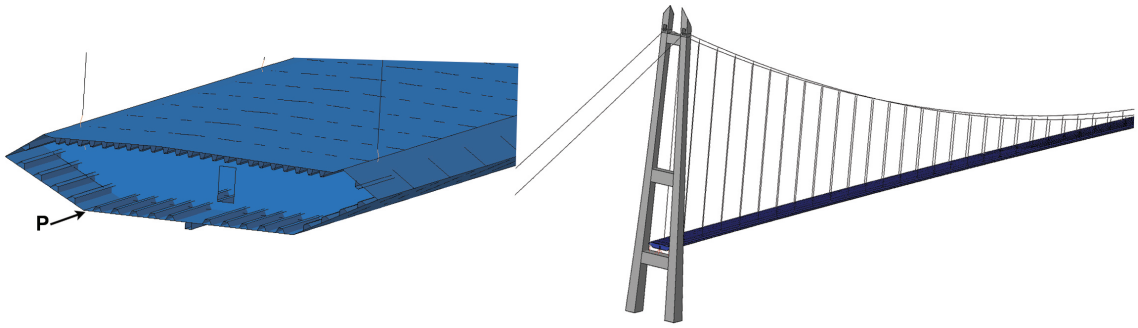

Fig. 6 Pictures of the FE model of the Hardanger Bridge.

$$\begin{bmatrix} \mathbf{A}-\lambda\mathbf{I} & \mathbf{B} \\ \mathbf{G} & \mathbf{J} \end{bmatrix} \begin{bmatrix} \mathbf{x}_0 \\ \mathbf{p}_0 \end{bmatrix} = \begin{bmatrix} \mathbf{0} \\ \mathbf{0} \end{bmatrix} \tag{16}$$

where $|\lambda| > 1$ and $|\lambda| < 1$ denote unstable and stable zeros, respectively. $\lambda = 1$ is the special case of marginal stability that always occurs when $\mathbf{S}_\mathrm{d} = \mathbf{0}$ [24]. In the case of acceleration output only ($\mathbf{S}_\mathrm{d} = \mathbf{0}$, $\mathbf{S}_\mathrm{a} \neq \mathbf{0}$), we experience that for most configurations of the state-space model (i.e. variations of the sensor network and modes in the system model), $\lambda = 1$ is present but no unstable zeros occur. Note that due to numerical precision, λ will strictly not be equal to unity; thus, its numerical value will fall in the stable or unstable region. This is normally not a significant issue unless data series with an extreme number of time steps are handled. Without installation of additional static-sensitive sensors, some practical options are available to overcome the problem of marginal stability:

(i) Use acceleration output only and accept the marginally stable zeros. The instability typically manifests as a low-frequency drift in the estimated states and forces, as observed by researchers in [2,20,21]. A high-pass filter can be applied to the time series in the post-processing of the results. A notable exception here is the DKF, which can avoid the drift under optimal regularization conditions.
(ii) Use both accelerations and displacements in the output vector, where the displacement data are synthesized by twice numerical integration of the accelerations and subsequently high-pass filtering to avoid the integration drift. This results in a stable system without zeros for our case.
(iii) Using dummy displacement measurements [26].

Options (i) and (ii) both imply a loss of information on any low-frequency behaviour due to the high-pass filtering. This can be a drawback for long-span bridges, where the wind-induced response can have some low-frequency components.

Invertibility. The direct invertibility requires that the rank of $\mathbf{J}$ is equal to the number of unknown forces [24]; thus, $\mathrm{rank}(\mathbf{S}_\mathrm{a}\boldsymbol{\Phi}) = \mathrm{n_m}$ when modal forces are used. This is a heavy implication for the number of modal loads that can be identified since a limited number of (linearly independent) acceleration measurements is available. As already discussed in Section 3.2 and shown in Fig. 5, a high number of modes contributes to the wind-induced response in suspension bridges.

3.4 Sensor network

The following outputs are included in the sensor network:

(i) The z-signals from all sensors in the girder, except H2W.
(ii) The y-signals from sensors H1E, H3E, H4E, H5E, H6E, H7E, H8E, H9E, T1E, and T2E.
(iii) The difference in x-signals from all sensor pairs in the girder, e.g. $u_{x,H1W}(t) - u_{x,H1E}(t)$ for the first pair. This output is proportional to the rotation about the z-axis at the local section.

The remainder of the signals are discarded either because they are redundant, too small in modal amplitude, or used as a reference output for validation. In total, 32 acceleration outputs are used. For the JIS, the displacement output obtained by numerical integration is also included; thus, $\mathrm{n_d} = 2 \times 32 = 64$. For the DKF, only acceleration output data are used ($\mathrm{n_d} = 32$).

3.5 System model

The modal system model should, from a practical perspective, represent the observed dynamics of the structure while also conforming to the theoretical requirements discussed in Section 3.3. The system vibration modes in Eq. 3 are obtained

Table 1 List of modes in the model and their correspondence with identified modal quantities denoted with an overbar. H=horizontal bending, V=vertical bending, T=torsion. MAC indicates the Modal Assurance Criterion

Mode no. j	Mode name	ω_j [rad/s]	$\bar{\omega}_j$ [rad/s]	$\bar{\xi}_j$ [%]	MAC($\boldsymbol{\phi}_j$, Re($\bar{\boldsymbol{\phi}}_j$))
1	H1	0.321	0.324	0.65	0.999
2	H2	0.657	0.663	0.77	0.993
3	V1	0.707	0.748	1.77	0.989
4	V2	0.890	0.893	0.65	0.995
5	H3	1.161	1.151	0.77	0.993
6	V3	1.273	1.294	0.27	0.992
7	V4	1.332	1.335	0.35	0.997
8	V5	1.737	1.735	0.26	0.998
9	H4	2.001	1.997	0.63	0.990
10	V6	2.088	2.093	0.25	0.995
11	T1	2.331	2.352	0.41	0.964
12	V7	2.517	2.519	0.24	0.997
13	H5	2.911	2.915	1.56	0.704
14	V8	2.938	2.960	0.26	0.991

from an FE model of the bridge pictured in Fig. 6. The global modal characteristics of suspension bridges from FE models generally have decent accuracy when the main bridge geometry is properly modelled and reasonable values for mass and stiffness are provided. Since it is desired to keep the model errors to a minimum, a high-fidelity model is employed, where shell elements are used for the girder and towers. In particular, this makes the torsional stiffness and inertia properties of the girder easier to model than for a beam model because the shell geometry avoids the need for conjectures on equivalent beam cross-section coefficients. Beam elements are used for the main cable and the hangers. The modes of the bridge below 6.3 rad/s or 1 Hz can generally be classified into three categories:

(i) Bending or torsion modes with a large girder response, i.e. shapes with a classic n-sine half-wave pattern. These are commonly regarded as the "main" modes of suspension bridges.
(ii) Modes with mainly cable response, which here are deemed insignificant because they are unobservable by the sensors.
(iii) Tower modes, which we also discard here.

Covariance-driven stochastic subspace identification (Cov-SSI) is used to estimate the true natural frequencies ($\bar{\omega}_j$), damping ratios ($\bar{\xi}_j$) and mode shapes ($\bar{\boldsymbol{\phi}}_j$) of the bridge in operational conditions with low wind velocity (3-6 m/s) so that still-air modal properties is a fair approximation; see [29] for details. It is assumed that the effect of small time-variations in the modal properties due to for example changes in temperature can be neglected. Note that in the system formulation used (Eq. 1 and 2), the aerodynamic stiffness and damping are considered as load effects, and so does not influence the still-air modal properties.

The FE model is calibrated in a classic sensitivity-based model updating scheme [29], with the objective of matching the mode shapes and natural frequencies of the model to the identified ones. Herein, the following model parameters are adjusted: the densities and elastic stiffnesses of the girder, towers and main cable; the non-structural mass on the girder; the shear stiffness of the girder; the hanger tension; and spring-elastic stiffnesses representing the bearings in the girder-tower connection.

The (updated) modes that are finally included in the state-space model are listed in Table 1 ($\mathrm{n_m} = 14$), together with the identified frequencies and damping ratios. Twelve of these modes are shown in Fig. 7. Most of the errors in natural frequencies are less than 1%, but a notable outlier is mode V1 ($\omega_3 = 0.707$ rad/s), which is underpredicted by 5.8%. In general, the mode shapes in the model also match well with the identified ones, as shown by the modal assurance criterion (MAC). The highest system frequency considered is $\omega_{14} = 2.94$ rad/s. A system model which includes even higher modes is found to be infeasible for use in the inverse algorithms, as it leads to an ill-conditioned system inversion and severe errors in the results. In accordance with the invertibility criterion in Section 3.3, a system with 14 modes is below the number of modal loads that could theoretically be identified. For a system model with more than 14 modes, however, the condition number of the matrix $\mathbf{J}$ $(= \mathbf{S}_\mathrm{a}\boldsymbol{\Phi})$ significantly increases, indicating close to linear dependencies in the acceleration data. This could be linked to the sensor layout, and again to the pairwise sensor allocation. In essence, a decisive modal cut-off here becomes an effort of trial and error, with the development of more generic guidelines considered as future work.

4 Response estimation results for the Hardanger Bridge

4.1 Measurement data

A set of six hours of continuous measurement data starting on the 29th of January, 2016, at 13:00 is utilized, corresponding to 36 consecutive ten minute events. These data are acquired during the "Storm Tor" striking Northern Europe and also the Norwegian west coast. The wind field characteristics at the Hardanger Bridge during this storm were investigated in [10],

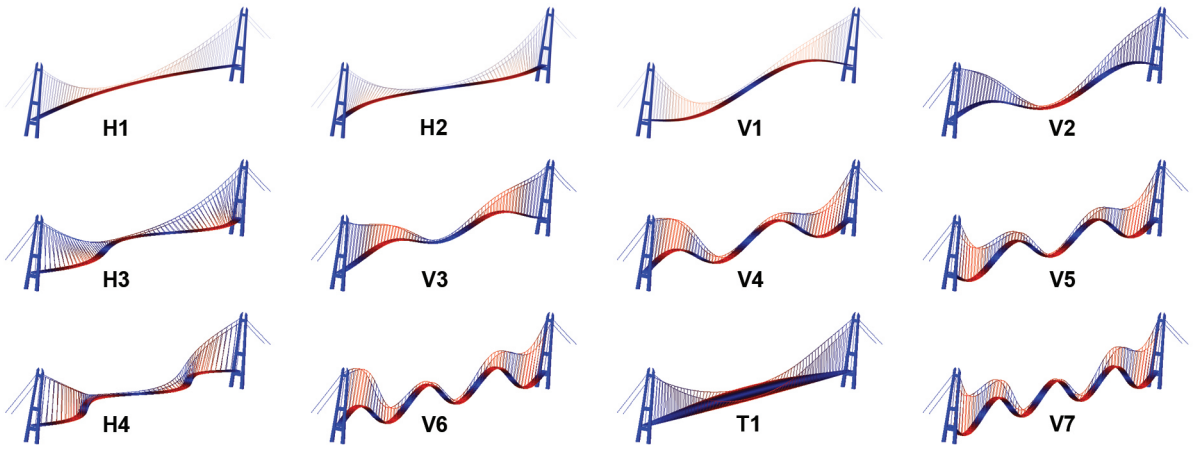

Fig. 7 A selection of twelve modes from the FE model

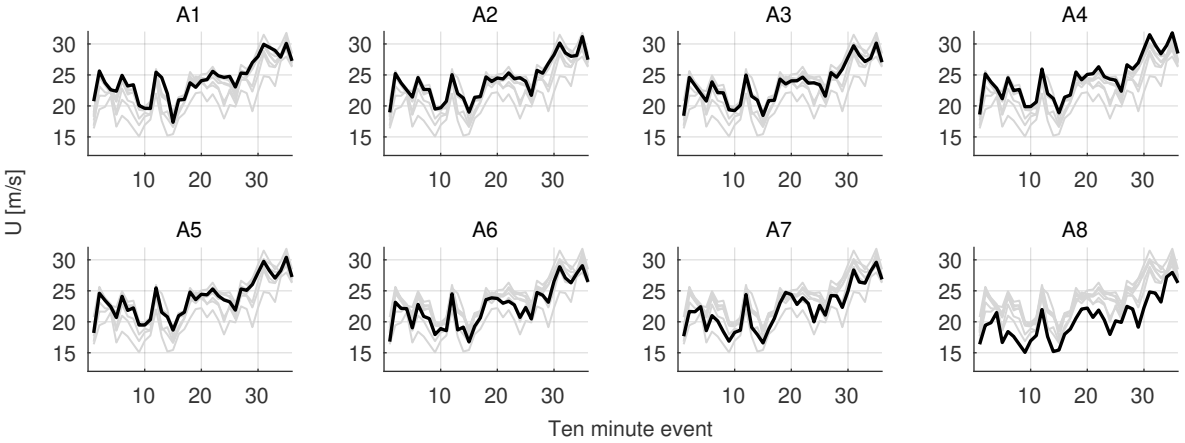

Fig. 8 Mean wind velocities for the six hour period recorded by anemometers A1-A8 located along the bridge span. The grey lines show all values for all anemometers, and the black line shows the values for the individual anemometer

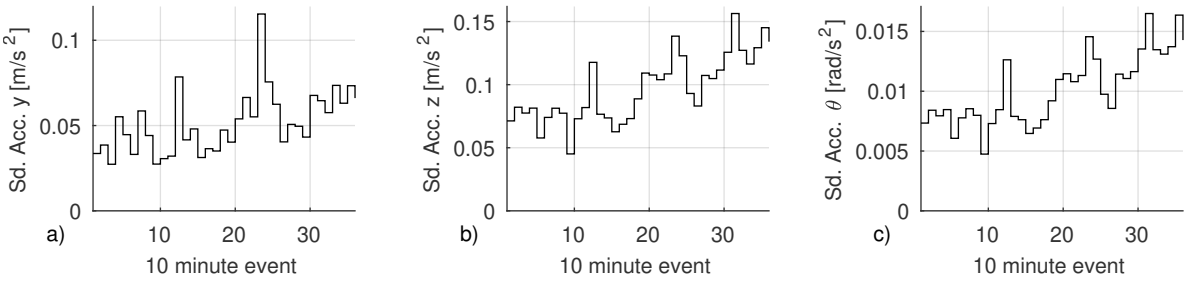

Fig. 9 Statistics of the 36 ten minute events: (a) mean and standard deviation of the along-wind velocity at anemometer A6. (b)-(d) show the standard deviations of the measured lateral, vertical and torsional acceleration responses at the mid-span.

where it was recognized that the wind recordings showed non-stationary features, although admitting that the testing for non-stationarity was not very robust. As shown in Fig. 8, the recorded mean wind velocities varied between 14.7 and 31.8 m/s in the considered six hour period. The measured response levels are also varying, as shown by the mid-span response statistics in Fig. 9.

The Chebychev II filters in Fig. 10 are applied to the output data, which are resampled to $\Delta t = 0.1$ s ($N_t = 216 \times 10^3$ time steps). It can be expected that the dynamics of the modes close to the cut-off frequency become slightly misrepresented since the natural frequencies of suspension bridges are very closely spaced and it is difficult to design a filter that fully includes the dynamics in the band of the highest mode of the model ($\omega_{14} = 2.94$ rad/s) but fully excludes the next modes. It is also important that the high-pass filter (Fig. 10b) has a narrow transition band to remove the low-frequency integration drift due to noise accumulation in the numerical integration, without removing the dynamic content in the band of the lowest mode ($\omega_1 = 0.32$ rad/s). As mentioned earlier, the lack of directly acquired static vibration data generally means that any information on the quasi-static behaviour is missing; thus, the analysis here focuses on the dynamics above 0.3

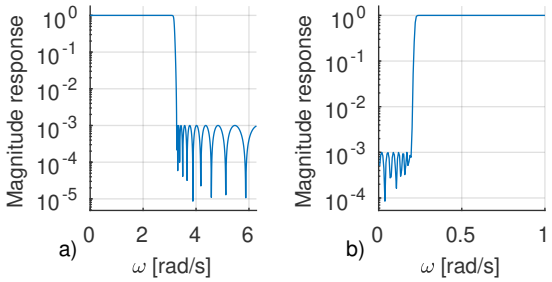

Fig. 10 Absolute values of the frequency-domain digital filter transfer functions: (a) low-pass filter applied to the output data, and (b) high-pass filter applied in the numerical time-integration

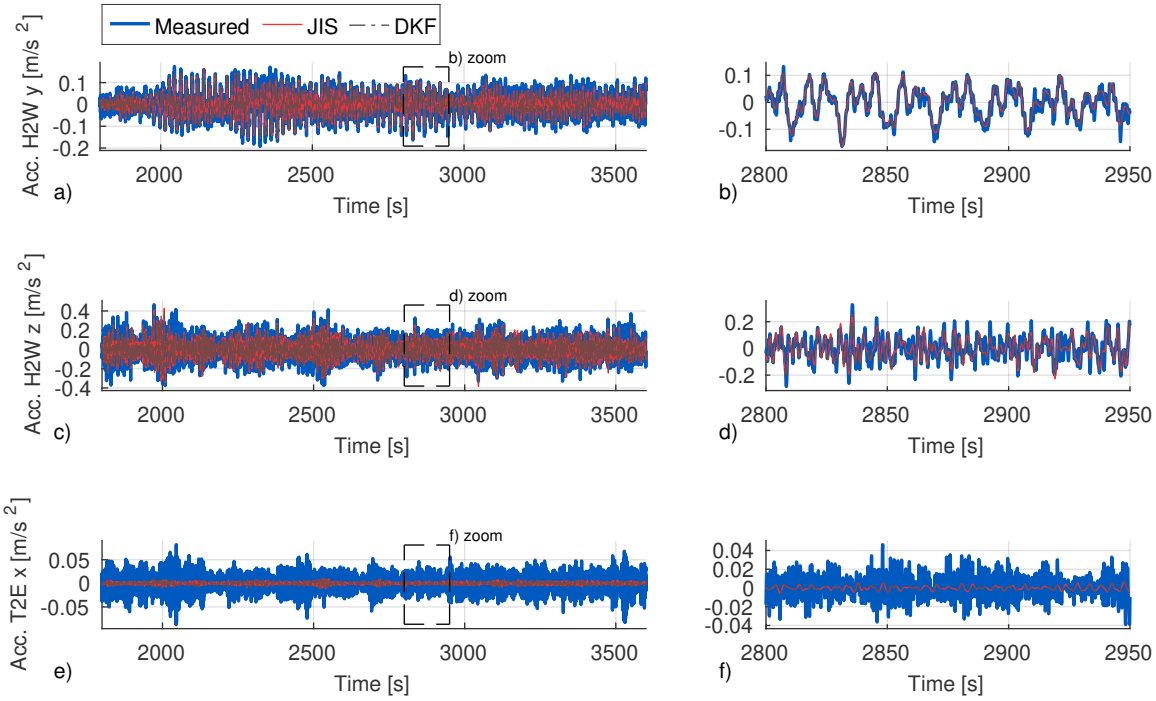

Fig. 11 Estimated and measured accelerations for the period $t \in [1800, 3600]$ s in (a) the lateral direction in the girder (H2W y), (c) the vertical direction in the girder (H2W z), and (e) the longitudinal direction in the tower (T2E x). The subfigures (b), (d) and (f) show time snippets of the three signals

rad/s. The pre-processing of the measurement data means that the filter applications here are not online; however, the data could still be processed in batches in an automated system after the acquisition.

4.2 Response prediction

The dynamic response of the bridge is now predicted at unmeasured locations using the two filtering algorithms in combination with Eq. 14. In the analysis, $\mathbf{Q}$ is set to $10^{-2} \times \mathbf{I}$. The measurement error covariance $\mathbf{R}$ is set to $10^{-6} \times \mathbf{I}$, corresponding to approximately 10^{-4} times the variance of the output signals. We observe that the first-order sensitivity of the solution with respect to these covariance matrices is generally low. The force step error covariance $\mathbf{Q}_{\mathrm{P}}$ is set to $10 \times \mathbf{I}$. This is the highest order that the parameter can attain before low-frequency drift occurs. More sophisticated calibration methods are also possible, but this parameter mostly influences the force magnitude rather than the states, which is mainly focused on here.

The signals H2Wy and H2Wz in the girder and T2Ex in the tower are used as a set of reference DOFs for the response prediction. Fig. 11 and Fig. 12 show the estimated accelerations at these 3 DOFs in the time domain for the thirty minutes $t \in [1800, 3600]$ s. To provide a realistic image of the actual performance obtained, the reference output data shown are not filtered. The estimated displacements in the same DOFs are also shown in Figs. 13 and 14. The estimates from the JIS and DKF are in general quite similar.

To characterize the time-domain error, the following root mean square (RMS) error metric is used for each reference output $d^{(i)}$:

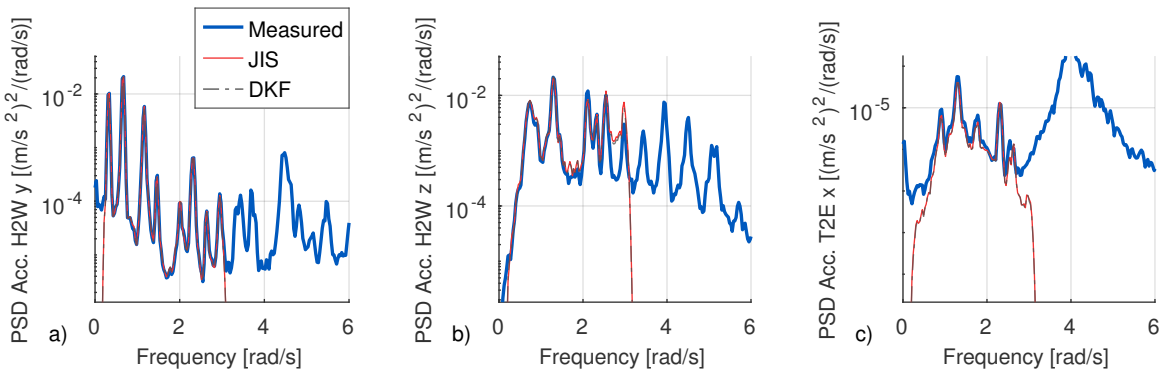

Fig. 12 PSD of estimated and measured accelerations for the period $t \in [1800, 3600]$ s in (a) the lateral direction in the girder (H2W y), (b) the vertical direction in the girder (H2W z), and (c) the longitudinal direction in the tower (T2E x)

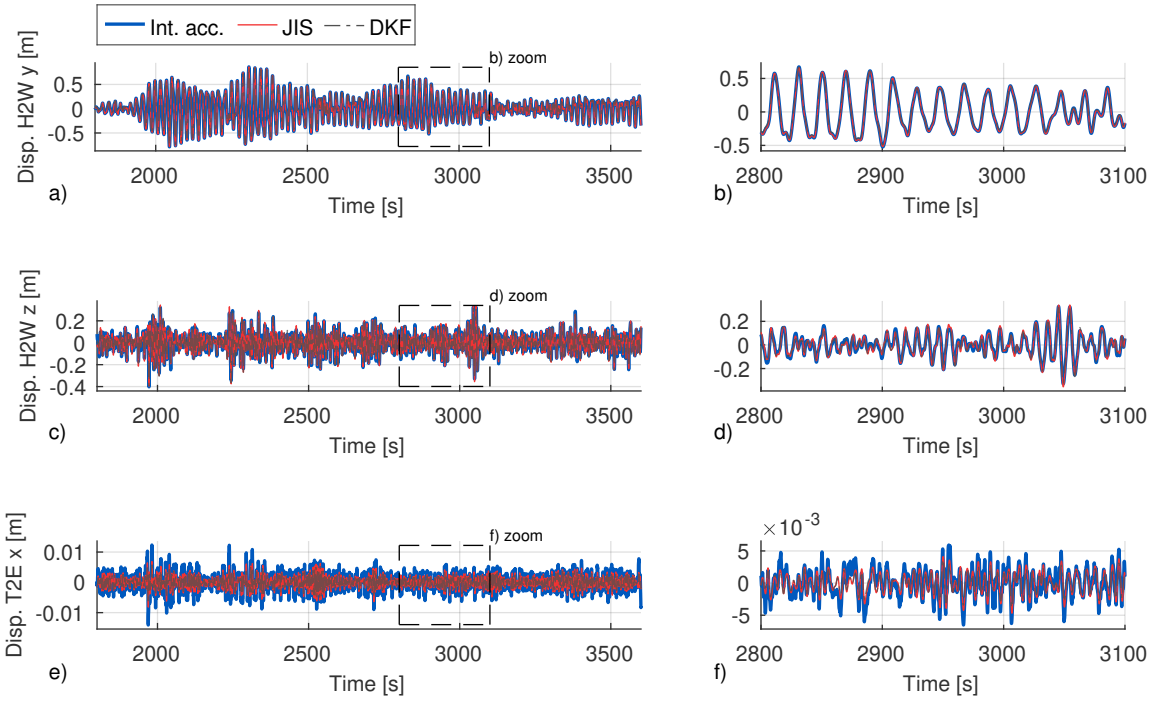

Fig. 13 Estimated and measured displacements for the period $t \in [1800, 3600]$ s in (a) the lateral direction in the girder (H2W y), (c) the vertical direction in the girder (H2W z), and (e) the longitudinal direction in the tower (T2E x). The subfigures (b), (d) and (f) show time snippets of the three signals

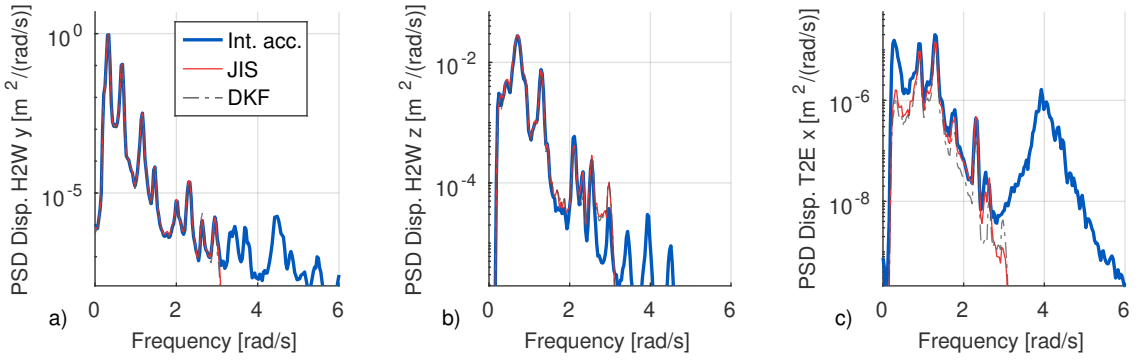

Fig. 14 PSD of estimated and measured displacements for the period $t \in [1800, 3600]$ s in (a) the lateral direction in the girder (H2W y), (b) the vertical direction in the girder (H2W z), and (c) the longitudinal direction in the tower (T2E x)

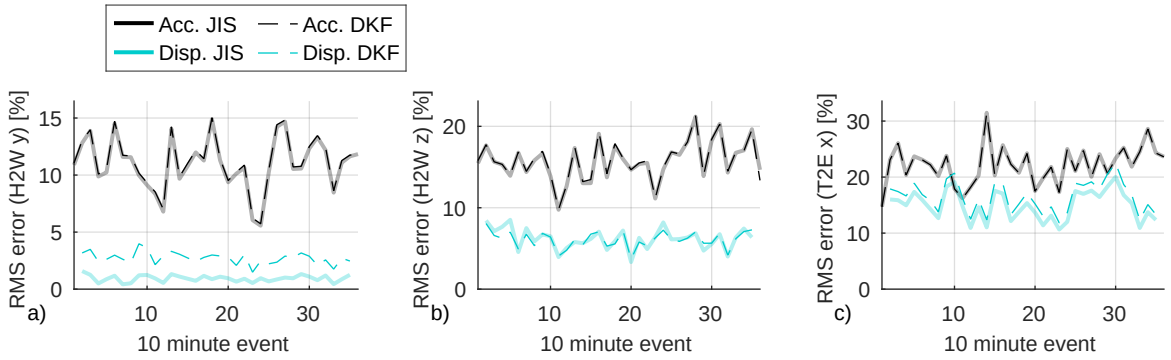

Fig. 15 RMS error in the predicted response in the three reference DOFs. The displacement errors for the first and last event are disregarded due to transient filter content

$$E_i = \sqrt{\frac{1}{N_t - 1} \sum_{k=0}^{N_t} \left(\frac{d_k^{(i)} - \hat{d}_k^{(i)}}{\max(|d^{(i)}|)} \right)^2} \tag{17}$$

Fig. 15 shows the RMS error for each event. Note that since both methods used (JIS and DKF) are time-recursive estimators, the length of the data analyzed generally does not influence the accuracy of the estimates or possible errors. Although some variations occur, the general error level can be observed. The accelerations consistently have larger errors than the displacements. As shown in Fig. 12, the frequency content above 3 rad/s cannot be reconstructed as this primarily originates from modes excluded from the model. The displacements (Fig. 14) are dominated by the lower modes and are thus more adequately reconstructed by filter estimates using a low-order model, leading to a lower error. For the towers, for example, the contribution from the lower modes is captured (Fig. 12c), but the accelerations are dominated by tower modes in the range 3-6 rad/s, which are not included in the model. In wind engineering, however, it is typically the dynamics of the bridge girder that is deemed most important, which appear to be well reconstructed.

It is clear that the response prediction works best in characterizing the global behaviour from a distributed network of sensors. As a counter example, in cable-stayed bridges, it is often the vortex-induced vibration of the cable stays that is the most critical concern with respect to early structural degradation or damage. The cable vibrations are a more local phenomenon and thus require more direct measurements to be properly reconstructed, although it has been demonstrated that the vortex-induced vibrations of the hangers at the Hardanger Bridge can be detected by the accelerometers as the high-frequency cable vibrations transmit down in the girder [5].

As an illustration, the longitudinal strain is also estimated in the girder (in the section point P, see Fig. 6) at the quarter ($x = 328$ m) and middle ($x = 0$ m) points of the span, as shown in Fig. 16. As a reference for comparison, the strain is calculated from the design basis of the bridge based on classical multi-mode theory of buffeting response in the frequency domain. The details behind this approach are provided in [9]. The most important equations and assumptions can be summarized as follows:

A stationary and homogeneous wind field is necessary to adopt here. The design wind spectrum $\mathbf{S}_{\text{vv}}(\omega, \Delta x) \in \mathbb{R}^{2\times 2}$ containing the along-wind and vertical wind velocity is of the Kaimal-type; see [9]. Only buffeting wind loads along the girder bridge span are included ($-L/2 \leq x \leq L/2, L = 1308$ m), which can be considered unconservative. The modal (design) buffeting load spectrum $\mathbf{S}_{\text{pp}}(\omega) \in \mathbb{R}^{\text{n}_\text{m}\times \text{n}_\text{m}}$ is calculated as follows:

$$\mathbf{S}_{\text{pp}}(\omega) = \int_{-L/2}^{L/2} \int_{-L/2}^{L/2} \mathbf{\Phi}_{\text{g}}(x_1)^{\text{T}} \mathbf{B}_{\text{q}} \mathbf{S}_{\text{vv}}(\omega, \Delta x) \mathbf{B}_{\text{q}}^{\text{T}} \mathbf{\Phi}_{\text{g}}(x_2)\, \text{d}x_1 \text{d}x_2 \tag{18}$$

This integral is evaluated by discretizing the span into equal segments of 4 m. The matrix $\mathbf{\Phi}_{\text{g}}(x) \in \mathbb{R}^{3\times \text{n}_\text{m}}$ contains the horizontal, vertical and pitching modal deflection of the girder along the span:

$$\mathbf{\Phi}_{\text{g}}(x) = \begin{bmatrix} \mathbf{\Phi}_y(x) \\ \mathbf{\Phi}_z(x) \\ \mathbf{\Phi}_\theta(x) \end{bmatrix} \tag{19}$$

The buffeting coefficient matrix $\mathbf{B}_{\text{q}} \in \mathbb{R}^{3\times 2}$, assumed to have frequency-independent admittance, is set to:

$$\mathbf{B}_{\text{q}} = \frac{\rho U B}{2} \begin{bmatrix} 2(D/B)\bar{C}_D & (D/B)C'_D - \bar{C}_L \\ 2\bar{C}_L & C'_L - (D/B)\bar{C}_D \\ 2B\bar{C}_M & BC'_M \end{bmatrix} \tag{20}$$

Table 2 Aerodynamic coefficients for the Hardanger Bridge obtained from wind tunnel experiments [31]

Parameter	Value
$\bar{C}_D$	1.05
C'_D	0
$\bar{C}_L$	-0.363
C'_L	2.22
$\bar{C}_M$	-0.017
C'_M	0.786
B	18.3 m
D	3.25 m
ρ	1.25 kg/m^3

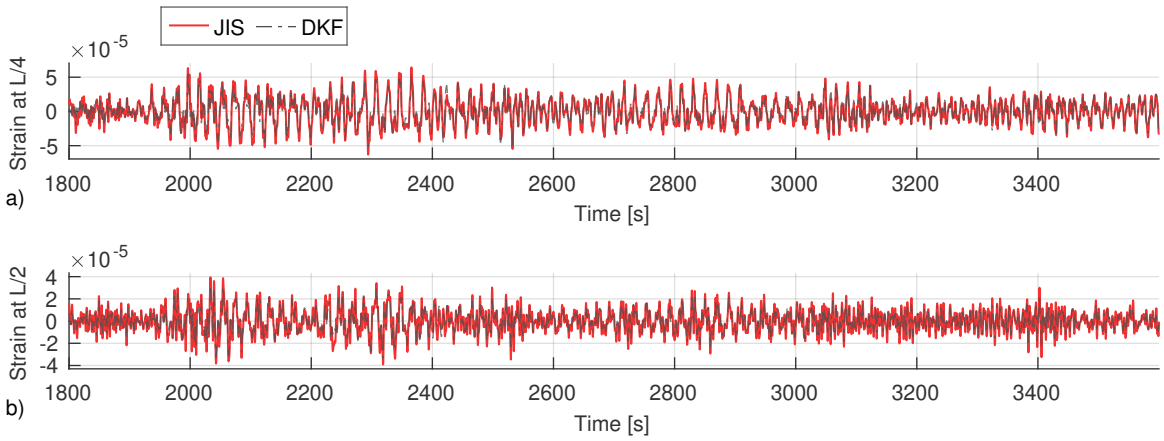

Fig. 16 Estimated strain at the (a) quarter-span, and (b) mid-span for the period $t \in [1800, 3600]$ s

where the coefficients are listed in Table 2. U is set as the mean wind velocity from anemometer A6 in the middle of the bridge. The modal transfer function $\mathbf{H}_{\text{pz}}(\omega) \in \mathbb{C}^{\text{n}_\text{m} \times \text{n}_\text{m}}$, taking aerodynamic damping and stiffness into account, is defined as:

$$\mathbf{H}_{\text{pz}}(\omega) = [-\omega^2 \mathbf{I} + i\omega(2\boldsymbol{\Xi}\boldsymbol{\Omega} - \tilde{\mathbf{C}}_{\text{ae}}) + \boldsymbol{\Omega}^2 - \tilde{\mathbf{K}}_{\text{ae}}]^{-1} \tag{21}$$

Quasi-steady theory is for simplicity assumed, meaning that the modal aerodynamic damping and stiffness become:

$$\tilde{\mathbf{C}}_{\text{ae}} = \int_{-L/2}^{L/2} \boldsymbol{\Phi}_{\text{g}}(x)^{\text{T}} \mathbf{C}_{\text{ae}} \boldsymbol{\Phi}_{\text{g}}(x)\, \text{d}x, \quad \tilde{\mathbf{K}}_{\text{ae}} = \int_{-L/2}^{L/2} \boldsymbol{\Phi}_{\text{g}}(x)^{\text{T}} \mathbf{K}_{\text{ae}} \boldsymbol{\Phi}_{\text{g}}(x)\, \text{d}x \tag{22}$$

$$\mathbf{C}_{\text{ae}} = -\frac{\rho U B}{2} \begin{bmatrix} 2(D/B)\bar{C}_D & (D/B)C'_D - \bar{C}_L & 0 \\ 2\bar{C}_L & C'_L - (D/B)\bar{C}_D & 0 \\ 2B\bar{C}_M & BC'_M & 0 \end{bmatrix}, \quad \mathbf{K}_{\text{ae}} = \frac{\rho U^2 B}{2} \begin{bmatrix} 0 & 0 & (D/B)C'_D \\ 0 & 0 & C'_L \\ 0 & 0 & BC'_M \end{bmatrix} \tag{23}$$

The modal response spectrum $\mathbf{S}_{zz}(\omega) \in \mathbb{C}^{\text{n}_\text{m} \times \text{n}_\text{m}}$ is then directly obtained:

$$\mathbf{S}_{\text{zz}}(\omega) = \mathbf{H}_{\text{pz}}(\omega)^{\text{H}} \mathbf{S}_{\text{pp}}(\omega) \mathbf{H}_{\text{pz}}(\omega) \tag{24}$$

The strain PSD matrix $\mathbf{S}_{\epsilon\epsilon}(\omega) \in \mathbb{C}^{\text{n}_\epsilon \times \text{n}_\epsilon}$ is calculated using the strain modes $\boldsymbol{\Phi}_\epsilon \in \mathbb{R}^{\text{n}_\text{DOF} \times \text{n}_\text{m}}$ at the n_ϵ locations selected by the matrix $\mathbf{S}_\epsilon \in \mathbb{R}^{\text{n}_\epsilon \times \text{n}_\text{DOF}}$:

$$\mathbf{S}_{\epsilon\epsilon}(\omega) = \mathbf{S}_\epsilon \boldsymbol{\Phi}_\epsilon \mathbf{S}_{\text{zz}}(\omega) \boldsymbol{\Phi}_\epsilon^{\text{T}} \mathbf{S}_\epsilon^{\text{T}} \tag{25}$$

Fig. 17 shows the (auto) PSDs of the strains for $t \in [1800, 3600]$ s. Here, modes above 2 rad/s also significantly contribute to the total strain because the curvature of the modal girder deflection increases with the square of the number of half-waves (Fig. 7). Generally, the filters predict a larger strain contribution from the horizontal modes H1, H2 and H3 than the design-based estimate. If the wind loading on the cables and towers were also considered in the design prediction, then a 10-20% increase in the response of the horizontal modes would be realistic [33]. For the vertical modes, there is a better correspondence but still some discrepancies for V1, V2 and V8. However, it is not expected that the presented spectra should be equal; the comparison is meant to show the variations that can be expected from the numerically predicted and real-life behaviour of the bridge. Overall, the spectral characteristics from the two approaches appear similar.

The standard deviation of the strain along the span in the same 30 minute period is shown in Fig. 18, which for the design prediction case can be calculated from the PSD matrix as the diagonal of $[\int_0^\infty \mathbf{S}_{\epsilon\epsilon}(\omega)\, \text{d}\omega]^{1/2}$. The JIS gives larger strains

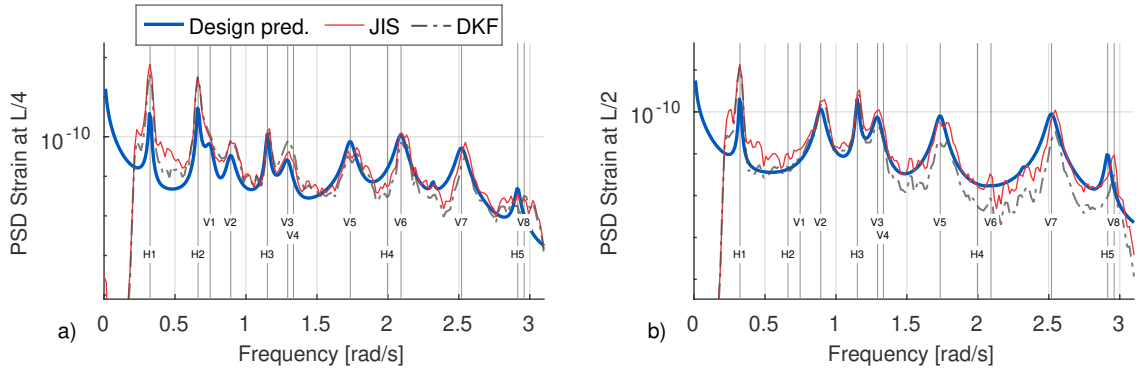

Fig. 17 The PSD of the strain from filter estimates and the design-based prediction at the (a) quarter span, and (b) mid-span for the period $t \in [1800, 3600]$ s. The vertical lines indicate the natural frequencies of the horizontal and vertical bending modes

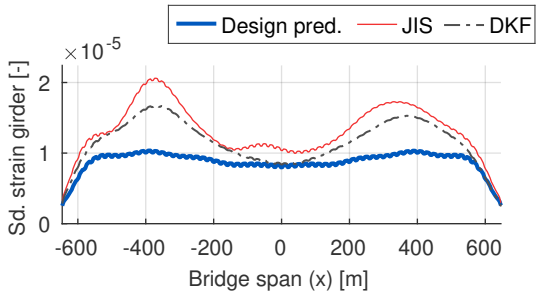

Fig. 18 Standard deviation of the girder strain along the span for the period $t \in [1800, 3600]$ s

than the DKF and also indicates a non-symmetric distribution along the span, which could be an artifact from estimation errors in the modal state vector. The DKF, which is the most moderate of the two estimates, still yields up to 50% higher strain levels than predicted. This result is consistent with the earlier studies of the Hardanger Bridge in the duration of the storm, finding that the measured RMS accelerations were higher than predicted for both the lateral, vertical and torsion responses [10]. The magnitude of the stresses are highly influential in fatigue assessments, so the full-field estimation could give a more certain prediction of possible fatigue damage.

An other point from observed from the measured wind data are inhomogenities in the wind field. For example, in Fig. 8 a consistent trend can be seen where mean wind velocities are decreasing from anemometer A1 to A8 by approximately 10-20%. Similar along-span variations can be seen for turbulence intensities. This shows a complexity of the wind field which is difficult to model with great certainty, and promotes the advantage of inverse response estimation, where the load model need not be known.

The observed discrepancies in Fig. 16-18 indicate that the response effects can be determined with greater confidence compared with the prediction from design specifications. A more accurate representation of the response will lead to improved assessment of the condition of the bridge, for example performance during strong winds, fatigue calculations or evaluation of serviceability. Still, it is recognized that the application of inverse methods to long-span bridges require further testing and development to ensure a robust performance.

4.3 Extensions of the research

A few points can be highlighted as possible extensions of this work:

(i) *Input estimation.* The research should be extended to input estimation of wind forces, assessing the identified forces in light of the wind measurements.

(ii) *Sensor network design.* The current sensor network can be improved, either by installing additional accelerometers or strain gauges.

(iii) *Model uncertainties.* Advancing the identification of the modal parameters to map the model uncertainties, for example, by tracking the variation of natural frequencies and damping over a longer period.

(iv) *Long-term response estimation.* An interesting study is to estimate the response for a longer period and evaluate how the response compares to the numerical (design) predictions under a variety of conditions, such as weak and strong winds,

inhomogeneous wind, skew wind or non-stationary wind. This requires some type of automated batch processing of the data while ensuring that the analysis is robust, which can be a challenge for the inverse-type problems.

5 Conclusion

This paper has presented the use of inverse methods for reconstruction of full-field responses in long-span cable-supported bridges from measured vibration data and a reduced-order system model. Two well-established Kalman-type filtering algorithms were used for the state and input estimation. The focus was on a case study of the Hardanger Bridge, a suspension bridge with uncertain wind conditions. The major advantage of the methodology is that an established model for the wind field or aerodynamic coefficients from wind tunnel experiments is not required, meaning the response effect uncertainties related to the load assumptions can be reduced.

The results from the case study show that full-field response estimation using measured acceleration data is feasible, with the limitation of only reconstructing the response contribution of the 14 modes below 3 rad/s (0.5 Hz) for the presented case. In particular, it was found that the typical multi-modal behaviour of suspension bridges represent an issue because the number of modal loads that can be identified are limited by the output data available. The practical use of the methods requires an extensive sensor network, where prior to instrumentation a study on optimization of the sensor network should preferably also be performed, which unfortunately was not possible here.

The response estimation could be helpful in assessments which requires the knowledge of various response effects in long-span bridges, e.g. wind-resistant performance, fatigue calculations, serviceability evaluation.

Acknowledgements This work was financially supported by the Norwegian Public Roads Administration, the E39 Coastal Highway Route project.

References

1. Azam, S.E., Chatzi, E., Papadimitriou, C.: A dual Kalman filter approach for state estimation via output-only acceleration measurements. Mechanical Systems and Signal Processing **60**, 866–886 (2015)
2. Azam, S.E., Chatzi, E., Papadimitriou, C., Smyth, A.: Experimental validation of the Kalman-type filters for online and real-time state and input estimation. Journal of Vibration and Control **23**(15), 2494–2519 (2015)
3. Bastos, F., Caetano, E., Cunha, Á., Cespedes, X., Flamand, O.: Characterisation of the wind properties in the Grande Ravine viaduct. Journal of Wind Engineering and Industrial Aerodynamics **173**, 112–131 (2018)
4. Brownjohn, J.M., De Stefano, A., Xu, Y.L., Wenzel, H., Aktan, A.E.: Vibration-based monitoring of civil infrastructure: challenges and successes. Journal of Civil Structural Health Monitoring **1**(3-4), 79–95 (2011)
5. Cantero, D., Øiseth, O., Rønnquist, A.: Indirect monitoring of vortex-induced vibration of suspension bridge hangers. Structural Health Monitoring p. 1475921717721873 (2017)
6. Chan, T.H., Li, Z., Ko, J.M.: Fatigue analysis and life prediction of bridges with structural health monitoring data - part ii: Application. International Journal of Fatigue **23**(1), 55–64 (2001)
7. Comanducci, G., Ubertini, F., Materazzi, A.L.: Structural health monitoring of suspension bridges with features affected by changing wind speed. Journal of Wind Engineering and Industrial Aerodynamics **141**, 12–26 (2015)
8. Deraemaeker, A., Reynders, E., De Roeck, G., Kullaa, J.: Vibration-based structural health monitoring using output-only measurements under changing environment. Mechanical systems and signal processing **22**(1), 34–56 (2008)
9. Fenerci, A., Øiseth, O.: Measured buffeting response of a long-span suspension bridge compared with numerical predictions based on design wind spectra. Journal of Structural Engineering **143**(9), 04017131 (2017)
10. Fenerci, A., Øiseth, O.: Strong wind characteristics and dynamic response of a long-span suspension bridge during a storm. Journal of Wind Engineering and Industrial Aerodynamics **172**, 116–138 (2018)
11. Fenerci, A., Øiseth, O., Rønnquist, A.: Long-term monitoring of wind field characteristics and dynamic response of a long-span suspension bridge in complex terrain. Engineering Structures **147**, 269–284 (2017)
12. Gu, M., Xu, Y., Chen, L., Xiang, H.: Fatigue life estimation of steel girder of yangpu cable-stayed bridge due to buffeting. Journal of Wind Engineering and Industrial Aerodynamics **80**(3), 383–400 (1999)
13. Hui, M., Larsen, A., Xiang, H.: Wind turbulence characteristics study at the Stonecutters Bridge site: Part i: Mean wind and turbulence intensities. Journal of Wind Engineering and Industrial Aerodynamics **97**(1), 22–36 (2009)
14. Iliopoulos, A., Shirzadeh, R., Weijtjens, W., Guillaume, P., Hemelrijck, D.V., Devriendt, C.: A modal decomposition and expansion approach for prediction of dynamic responses on a monopile offshore wind turbine using a limited number of vibration sensors. Mechanical Systems and Signal Processing **68-69**, 84–104 (2016)
15. Iliopoulos, A., Weijtjens, W., Van Hemelrijck, D., Devriendt, C.: Fatigue assessment of offshore wind turbines on monopile foundations using multi-band modal expansion. Wind Energy **20**(8), 1463–1479 (2017)
16. Ko, J., Ni, Y.: Technology developments in structural health monitoring of large-scale bridges. Engineering structures **27**(12), 1715–1725 (2005)
17. Ko, J., Ni, Y., Zhou, H., Wang, J., Zhou, X.: Investigation concerning structural health monitoring of an instrumented cable-stayed bridge. Structures & Infrastructure Engineering **5**(6), 497–513 (2009)
18. Li, H., Ou, J.: The state of the art in structural health monitoring of cable-stayed bridges. Journal of Civil Structural Health Monitoring **6**(1), 43–67 (2016)
19. Lourens, E., Fallais, D.: Full-field response monitoring in structural systems driven by a set of identified equivalent forces. Mechanical Systems and Signal Processing **114**, 106–119 (2019)
20. Lourens, E., Papadimitriou, C., Gillijns, S., Reynders, E., De Roeck, G., Lombaert, G.: Joint input-response estimation for structural systems based on reduced-order models and vibration data from a limited number of sensors. Mechanical Systems and Signal Processing **29**, 310–327 (2012)
21. Lourens, E., Reynders, E., De Roeck, G., Degrande, G., Lombaert, G.: An augmented Kalman filter for force identification in structural dynamics. Mechanical Systems and Signal Processing **27**, 446–460 (2012)

22. Maes, K., Gillijns, S., Lombaert, G.: A smoothing algorithm for joint input-state estimation in structural dynamics. Mechanical Systems and Signal Processing **98**, 292–309 (2018)
23. Maes, K., Iliopoulos, A., Weijtjens, W., Devriendt, C., Lombaert, G.: Dynamic strain estimation for fatigue assessment of an offshore monopile wind turbine using filtering and modal expansion algorithms. Mechanical Systems and Signal Processing **76-77**, 592–611 (2016)
24. Maes, K., Lourens, E., Van Nimmen, K., Reynders, E., De Roeck, G., Lombaert, G.: Design of sensor networks for instantaneous inversion of modally reduced order models in structural dynamics. Mechanical Systems and Signal Processing **52**, 628–644 (2014)
25. Maes, K., Smyth, A., De Roeck, G., Lombaert, G.: Joint input-state estimation in structural dynamics. Mechanical Systems and Signal Processing **70–71**, 445–466 (2016)
26. Naets, F., Cuadrado, J., Desmet, W.: Stable force identification in structural dynamics using Kalman filtering and dummy-measurements. Mechanical Systems and Signal Processing **50**, 235–248 (2015)
27. Ni, Y.Q.: Structural health monitoring of cable-supported bridges based on vibration measurements. Proceedings of the 9th International Conference on Structural Dynamics, EURODYN 2014 (2014)
28. Nord, T.S., Øiseth, O., Lourens, E.: Ice force identification on the Norströmsgrund lighthouse. Computers & Structures **169**, 24–39 (2016)
29. Petersen, Ø.W., Øiseth, O.: Finite element model updating of a long span suspension bridge. In: R. Rupakhety, S. Olafsson, B. Bessason (eds.) Proceedings of the International Conference on Earthquake Engineering and Structural Dynamics, pp. 335–344. Springer International Publishing, Cham (2019)
30. Petersen, Ø.W., Øiseth, O., Lourens, E.: Estimation of the dynamic response of a slender suspension bridge using measured acceleration data. Procedia Engineering **199**, 3047–3052 (2017)
31. Siedziako, B., Øiseth, O., Rønnquist, A.: An enhanced forced vibration rig for wind tunnel testing of bridge deck section models in arbitrary motion. Journal of Wind Engineering and Industrial Aerodynamics **164**, 152–163 (2017)
32. Skafte, A., Kristoffersen, J., Vestermark, J., Tygesen, U.T., Brincker, R.: Experimental study of strain prediction on wave induced structures using modal decomposition and quasi static ritz vectors. Engineering Structures **136**, 261–276 (2017)
33. Sun, D., Xu, Y., Ko, J., Lin, J.: Fully coupled buffeting analysis of long-span cable-supported bridges: formulation. Journal of sound and vibration **228**(3), 569–588 (1999)
34. Wang, H., Hu, R., Xie, J., Tong, T., Li, A.: Comparative study on buffeting performance of Sutong Bridge based on design and measured spectrum. Journal of Bridge Engineering **18**(7), 587–600 (2012)
35. Wang, H., Li, A., Niu, J., Zong, Z., Li, J.: Long-term monitoring of wind characteristics at Sutong Bridge site. Journal of Wind Engineering and Industrial Aerodynamics **115**, 39–47 (2013)
36. Xu, Y., Liu, T., Zhang, W.: Buffeting-induced fatigue damage assessment of a long suspension bridge. International Journal of Fatigue **31**(3), 575–586 (2009)
37. Xu, Y.L.: Making good use of structural health monitoring systems of long-span cable-supported bridges. Journal of Civil Structural Health Monitoring **8**(3), 477–497 (2018)
38. Ye, X., Ni, Y., Wong, K., Ko, J.: Statistical analysis of stress spectra for fatigue life assessment of steel bridges with structural health monitoring data. Engineering Structures **45**, 166–176 (2012)
39. Ye, X., Xi, P., Su, Y., Chen, B., Han, J.: Stochastic characterization of wind field characteristics of an arch bridge instrumented with structural health monitoring system. Structural safety **71**, 47–56 (2018)
40. Zhang, C., Xu, Y.: Optimal multi-type sensor placement for response and excitation reconstruction. Journal of Sound and Vibration **360**, 112–128 (2015)
41. Zhi, L., Li, Q., Fang, M.: Identification of wind loads and estimation of structural responses of super-tall buildings by an inverse method. Computer-Aided Civil and Infrastructure Engineering **31**(12), 966–982 (2016)